International Gas Union Research Conference 2011

# Development of Finite Element Based Defect Assessment Method for Gas Pipelines subject to Operating Condition Changes

Woosik Kim*, Jonghyeon Baek*, Yunjae Kim**

*KOGAS, **KOREA University

## ABSTRACT

Assessment methodology of structural integrity of gas pipeline is very important. For assessment of gas pipeline, many tests under various conditions have to be done. But test of real gas pipe is very dangerous and expensive. The objectives of this study are to develop micro-mechanical model for assessment of structural integrity of natural gas pipeline and develop damage model for assessment of defects in pipeline. We developed phenomenological damage simulation method for assessment of failure of natural gas pipeline, and developed user-subroutines in ABAQUS for implementation.

This paper proposes a new method to simulate ductile failure using finite element analysis based on the stress-modified fracture strain model. A procedure is given to determine the stress-modified fracture strain as a function of the stress triaxiality from smooth and notched bar tensile tests with FE analyses. For validation, simulated results using the proposed method are compared with experimental data for cracked bar (tensile and bend) tests, extracted from API X65 pipes, and for full-scale burst test of gouged pipes, showing overall good agreements. Advantages in the use of the proposed method for practical structural integrity assessment of natural gas pipeline are discussed.

# TABLE OF CONTENTS

## 1. INTRODUCTION

For structural integrity analyses of natural gas pipeline, performing full-scale tests is important, but is in general quite expensive and time consuming. Furthermore, it is often very difficult to perform full-scale tests reflecting complex geometries and loading conditions in practical assessment. For these reasons, an efficient tool may be needed not only to design complex full-scale tests but also possibly to minimize expensive and time-consuming full-scale tests. Finite element ductile failure simulations based on the local approach are quite useful in this respect and increasingly important.

A number of works have been reported in the literature up to present on finite element ductile failure simulations. Depending on the model employed for simulating damage, existing works can be broadly classified into two categories. The first one is using a micro-mechanical model for ductile fracture, incorporating void nucleation, growth and coalescence, for instance, GTL model [1, 2]. The second category is using a phenomenological model for ductile fracture, for instance, cohesive zone model [3, 4]. Applicability and validity of these methods have been well discussed in the literature.

From the author's point of view, it is felt that a few issues need to be resolved in practical application of these methods. The first one is how to find parameters embedded in these models. For instance, the GTN model has eight parameters related to micro-mechanism of ductile fracture. Determination of these parameters are not an easy task, and often not robust. Although other models tend to have less parameter, robust parameter determination is a common problem in finite element ductile failure simulations. The second issue is that, when these methods are to be implemented into commercial finite element programs, special subroutines or elements often need to be developed. This paper proposes a new method to simulate ductile failure using finite element method, based on a phenomenological stress-modified fracture strain model for ductile fracture.

## 2. EXPERIMENAL METHOD AND RESULTS

Tests were performed to show how to apply the proposed method to simulate ductile failure, and to validate the proposed method by comparing with experimental data. These tests include smooth and notched bar tensile tests, cracked bar tests and full-scale burst tests of gouged pipes. The material is the API X65 steel popularly used for natural gas transportation in Korea. Chemical composition and tensile properties of the API X65 steel is given in Table 1.

### 2.1. Smooth and notched round bar tensile tests

Standard round bar specimens for tensile tests were extracted in the longitudinal direction from API X65 pipe having outer diameter 762 mm and wall thickness 17.5 mm. To investigate the effect of triaxial stress states on tensile properties, notched round bar specimens with three different notch radii, 6.0 mm, 3.0 mm and 1.5 mm, were also made. For all specimens, the minimum section has a diameter of 6.0 mm. Schematic diagrams for smooth and notched round tensile specimens are depicted in Fig. 1. In tensile testing, axial displacement was monitored using extensometer with the gauge length of 25 mm. For a given specimen geometry, tests were repeated three times. Engineering

stress–strain data from all tests are shown in Fig. 2a. Yield and tensile strengths determined from smooth bar tensile tests were about 465 MPa and 563 MPa, respectively. True stress–strain data, obtained from smooth round bar tests are shown in Fig. 2b. The true fracture strain is about 1.2, indicating that the material is sufficiently ductile. Notched bar tests show that, as the notch radius decreases, the yield and tensile strengths increase, but the strain to fracture decreases due to the higher stress triaxialties introduced by the notch.

### 2.2. Cracked bar tests

To investigate constraint effects due to the loading mode on failure behaviors, single edge cracked bend specimen SE(B) for three-point bending loading and single-edge cracked tension specimen SE(T) for tensile loading were extracted from API X65 pipes as shown in Fig. 3. An initial notch was machined and the subsequent pre-cracking was introduced by fatigue. No side-groove was made for all specimens. For SE(B) specimens, the final crack length was about 50% of the width. The crack mouth opening displacement (CMOD) was monitored as a function of load. Load-CMOD curves resulting from two identical specimens are shown in Fig. 4a. For SE(T) specimens, the final crack lengths were about 25%, 50% and 75% of the width, to see the effect of the crack length on failure behaviors. The displacement was monitored using the extensometer with 10 mm gauge length. Resulting load–displacement curves are summarized in Fig. 4b. It shows that overall behaviors for SE(T) specimens are quite different from those for SE(B) ones.

### 2.3. Burst tests of full-scale pipes with gouge defect

To simulate gouge defect, a 45$^{o}$ V-notch with a circular notch radius of 2 mm was made on the outer surface of the pipe with the total length of 2300 mm. The depth of the gouge was fixed as 8.75 mm which is 50% of the pipe thickness. The axial length of the gouge was systematically varied from $l$ = 100 mm to $l$ = 600 mm (Table 2). Both ends were capped by circumferential welding. The pipes were pressurized by water and burst pressures were experimentally determined at the point when the ligament failed. Fig. 5 depicts photos of the gouge before and after the test. The measured maximum burst pressures from full-scale pipe tests are summarized in Table 2, which shows that the burst pressure decreases with increasing gouge length.

## 3. Proposed ductile failure simulation method

### 3.1. Damage model and failure simulation

The damage model proposed in this paper is based on the concept of the stress-modified fracture strain model. It has been well-known that fracture strain $\varepsilon_f$ for dimple fracture strongly depends on the stress triaxiality defined by the ratio of the mean normal stress $\sigma_m$ and equivalent stress $\sigma_e$ [5, 6]:

$$\frac{\sigma_m}{\sigma_e} = \frac{\sigma_1 + \sigma_2 + \sigma_3}{3\sigma_e} \quad (1)$$

$$\sigma_e = \sqrt{\frac{1}{2}\{(\sigma_1 - \sigma_2)^2 + (\sigma_1 - \sigma_3)^2 + (\sigma_3 - \sigma_2)^2\}} \quad (2)$$

Where $\sigma_i$ (i = 1–3) denotes the principal stress. The dependence of $\varepsilon_f$ on the stress triaxiality can be modeled using an exponential function

$$\varepsilon_f \propto \exp\left(-\alpha \frac{\sigma_m}{\sigma_e}\right) \quad (3)$$

Where α is a material constant. A detailed form of the fracture strain can be found from notched bar tensile tests. Once the form of $\varepsilon_f$ is available as a function of the stress triaxiality, incremental damage due to plastic deformation, Δω, is calculated using

$$\Delta\omega = \frac{\Delta\varepsilon_p}{\varepsilon_f} \quad (4)$$

Where $\Delta\varepsilon_p$ is the equivalent plastic strain increment, calculated from FE analysis.

When the accumulated damage becomes unity, $\omega = \Sigma\Delta\omega = 1$, ductile failure is assumed and incremental crack growth is simulated by reducing all stress components at the gauss point sharply to a small plateau value, as schematically depicted in Fig. 6. Decreasing stresses to zero can cause numerical problems, and thus stresses are assumed to remain a finite value.

### 3.2. Implementation to FE program ABAQUS

Suppose the fracture strain $\varepsilon_f$ is determined for a given material. Then damage simulation using the proposed method requires information on the stress triaxiality and incremental plastic strain values, which can be determined from elastic–plastic FE analysis. Thus the proposed method can be easily implemented in commercial FE programs. To implement the proposed damage model to ABAQUS [7], two user subroutines were developed. The first one is the USDFLD subroutine to re-define field variables. By defining as state variables, information on the mean normal stresses and equivalent stresses/strains at gauss points is passed into the UHARD subroutine. In the UHARD subroutine, accumulated damage is calculated according to Eq. (4) using information passed from the USDFLD subroutine. When the accumulated damage becomes critical, stresses are relaxed simply by changing the yield surface.

### 3.3. Determination of fracture strain $\varepsilon_f$

To apply the present damage model, the first step is to determine the fracture strain $\boldsymbol{\varepsilon_f}$ as a function of the stress triaxiality. Elastic–plastic, axi-symmetric FE analyses simulating tensile tests of smooth and notched round bar specimens were performed to determine variations of the triaxial stresses and strains within the specimens. Symmetric conditions were fully utilized and the second order, reduced integration elements were used for efficient computation. Typical FE meshes with the different notch radii are shown in Fig. 7. The number of elements and nodes in typical FE meshes ranged from 484 elements/1557 nodes to 658 elements/2089 nodes. To incorporate the large geometry change effect in tensile testing, the large geometry change option was chosen.

Fig. 8 compares experimental engineering stress–strain data from smooth and notched tensile tests with the FE results. Although the FE analysis cannot reproduce failure of tensile test specimens, it can well simulate deformation behavior even after necking up to failure initiation points. Agreements between the test results and FE ones are quite good up to failure initiation points which are indicated in Fig. 8 using the cross symbols.

Local stress and strain fields in the minimum section of the tensile bars were extracted from the FE results as a function of applied load. Fig. 9 shows radial variations of the stress triaxiality $\sigma_m/\sigma_e$ and equivalent strain $\varepsilon_e$ in the minimum section of the smooth and notched bars at the point of failure initiation. The equivalent strain, $\varepsilon_e$, is defined by

$$\varepsilon_e = \frac{\sqrt{2}}{3}\sqrt{\{(\varepsilon_1-\varepsilon_2)^2+(\varepsilon_1-\varepsilon_3)^2+(\varepsilon_3-\varepsilon_2)^2\}} \tag{5}$$

where $\varepsilon_i$ (i = 1–3) denotes the principal strain. In the figure, the distance (r) is normalized with respect to the radius of the minimum section (R), and the values of r/R = 0 and r/R = 1 mean the center and the free surface of the specimen, respectively. The stress triaxiality decreases with increasing notch radius, but always attains its maximum value in the center of the specimen, regardless of the notch radius. Furthermore, equivalent strain attains its maximum value in the center of the bar, except for the 1.5 mm case where the maximum value of equivalent strain occurs at the notch tip. Thus for all cases except for the 1.5 mm case, failure is expected to initiate in the center of the minimum section in the specimen. Even for the 1.5 mm case, as the stress triaxiality in the center is much higher than that in the notch tip, failure is also expected to initiate in the center of the minimum section in the specimen.

Fig. 10a shows the evolution of the stress triaxiality in terms of the equivalent strain for smooth and notched round tensile bars in solid lines. Both the stress triaxiality and the equivalent strain are extracted in the center of the minimum section of test specimens, where failure initiation is expected to occur. The last points in Fig. 10a correspond to the failure initiation points. It shows that the stress triaxiality in the center of the specimen depend on the equivalent strain. As a ductile failure criterion should include the history of stress and strain, average stress triaxiality is introduced, defined by

$$\left(\frac{\sigma_m}{\sigma_e}\right)_{ave} = \frac{1}{\varepsilon_{ef}}\int_0^{\varepsilon_{ef}} \frac{\sigma_m}{\sigma_e} d\varepsilon_e \tag{6}$$

where $\varepsilon_{ef}$ denotes the equivalent strain to failure initiation. Such definition can incorporate the history effect on stresses and strains on ductile fracture. For a given notch radius, the calculated average stress triaxiality is constant, and is shown in Fig. 10a with dotted lines. Resulting equivalent strains to failure initiation are shown in Fig. 10b, as a function of the stress triaxiality. One point in Fig. 10b corresponds to the result for one notch radius. It shows that the fracture strain decreases sharply with increasing the stress triaxiality. The fracture strain is found to be exponentially dependent on the stress triaxiality [8], the following regression is proposed for the fracture strain $\varepsilon_f$ :

$$\varepsilon_f = 3.29\exp\left(-1.54\frac{\sigma_m}{\sigma_e}\right)+0.10 \tag{7}$$

which is shown in Fig. 11b with a solid line. It shows that Eq. (7) agrees with the data and captures

dependence of the stress triaxiality on equivalent strain to fracture.

## 4. Results

### 4.1. Sensitivity analysis

To apply the proposed model to simulate ductile failure, first-order elements (the four-node quadrilateral element for two dimensional and axi-symmetric problems and the eight-node brick element for three-dimensional problems) with full integrations are used. The mesh size effect on simulated results was not investigated, and the size was fixed to 0.15 mm.

To investigate the effects of the decreasing slope and the cut-off value on simulated results, sensitivity analysis was performed for the cracked bars. For efficient investigations, two dimensional simulations were performed. Simulated load–displacement records for SE(B) and SE(T) specimens are compared with experimental data in Fig. 11. It shows that simulated results do not depend on the decreasing slope and the cut-off value, as long the decreasing slope was taken to be smaller than 1/5000 (when the strain increases by 0.1, the stress decreases more than 500 MPa) and the cut-off value is less than 50 MPa. Although the decreasing slope and cut-off value should be ideally zero, such values can cause numerical problems. Thus, for numerical efficiency, the cut-off value and decreasing slope were taken to be 10% of the yield strength and 1/5000, respectively.

### 4.2. Cracked bar test results

For comparison with cracked bar test results, 3-D FE analyses were performed because the tested cracked bars do not have any side-groove. Eight-node brick elements with full integrations (element type C3D8) of the size 0.15 mm x 0.15 mm x 15 mm were uniformly spaced in the cracked section. True stress–strain data were directly given in the FE analysis, and incremental plasticity with the large geometry change option was invoked. Fig. 12 compares cracked bar test results with simulated FE results. Deviations of the conventional elastic–plastic FE results from experimental data are due to crack growth. The proposed method gives overall good predictions for all cases considered, and agreements with experimental data are overall slightly better than those for the GTN model.

### 4.3. Burst tests of full-scale pipes with gouge defect

Burst tests of full-scale pipes with gouge defects are simulated using FE analyses. Eight-node brick elements with full integrations (element type C3D8) of the size 0.15 mm x 0.15 mm x 15 mm were uniformly spaced in the defective section. Internal pressure was applied to the inner surface of the pipe, with end forces to simulate the closed end condition. True stress–strain data were directly given in the FE analysis, and incremental plasticity with the large geometry change option was invoked.

Fig. 13a shows simulated pressure–displacement curves of gouged pipes. The displacement d is measured at the gouge mouth. Estimated burst pressures from the proposed method are compared with experimentally measured data in Fig. 13b. The estimated burst pressures are in good agreement with experimentally measured ones with differences less than about 3%, except the MNC case where

the difference is as much as about 12%. Although such a difference is still not significant, the experimental data for the MNC case are somewhat lower than expected from the trend curve.

## 5. Summary

A new method to simulate ductile failure based on FE analysis is proposed. The method is based on the stress-modified fracture strain model which has been well-known phenomenological model for ductile fracture. Incremental damage is defined by the ratio of incremental plastic strain and stress-modified fracture strain. When the accumulated damage becomes unity, then stresses at the gauss point are decreased to a small value to simulate progressive failure. To validate the proposed method, tests are performed using specimens extracted from API X65 grade pipes. The stress-modified fracture strain as a function of the stress triaxiality is firstly obtained by combining FE analyses and experimental data of smooth and notched bar tensile tests. Then simulated results using the proposed method are then compared with experimental data from cracked bar tests and full-scale burst test of gouged pipes. Good comparisons with experimental results support the confidence of the proposed method.

The proposed method adopts the stress-modified fracture strain model as a failure criterion for ductile fracture. Using notched bar tensile tests, determination of the stress-modified fracture strain model for a given material is straightforward and robust. Once the stress-modified fracture strain model is determined, the proposed damage model does not include any parameter and thus does not require any calibration procedure, which offers significant advantage in practical application.

## 6. References

[1] Gurson AL. Continuum theory of ductile rupture by void nucleation and growth. Part 1-yield criteria and flow rules for porous ductile media. J Eng Mater Tech, 1977, 99, pp2–15.

[2] Tvergaard V. Influence of voids on shear band instabilities under plane strain conditions. Int J Fract, 1981, 17, pp389–407.

[3] Chen CR, Kolednik O, Scheider I, Siegmund T, Tatschl A, Fischer FD. On the determination of the cohesive zone parameters for the modeling of microductile crack growth in thick specimens. Int J Fract, 2003, 120, pp517–36.

[4] Chen CR, Kolednik O, Heerens J, Fischer FD. Three dimensional modeling of ductile crack growth: cohesive zone parameters and crack tip triaxiality. Eng Fract Mech, 2005, 72, pp2072–94.

[5] McClintock FA. A criterion of ductile fracture by the growth of holes. J Appl Mech, 1968, 35, pp363–71.

[6] Hancock JW, Mackenzie AC. On the mechanisms of ductile failure in high-strength steels subject to multi-axial stress states. J Mech Phys Solids, 1976, 24, pp147–69.

[7] ABAQUS Version 6.7. User's manual, 2007.

[8] Rice JR, Tracey DM. On the ductile enlargement of voids in triaxial stress fields. J Mech Phys Solids, 1969, 17, pp201–17.

Table 1 Chemical compositions and mechanical tensile properties at room temperature of the API X65 steel, used in the present work

| Young's modulus | Poisson's ratio | Yield strength | Tensile strength | Element (wt %) | | | | | | |
|---|---|---|---|---|---|---|---|---|---|---|
| $E$ (GPa) | $n$ | $s_y$ (MPa) | $s_u$ (MPa) | C | P | Mn | S | Si | Fe | Ceq |
| 210.7 | 0.3 | 464.5 | 563.8 | 0.08 | 0.019 | 1.45 | 0.03 | 0.31 | Bal. | 0.32 |

Table 2 Summary of full-scale tests of pipes with gouge defect.

| Pipe no. | L (mm) | d (mm) | Burst pressure (MPa) |
|---|---|---|---|
| MNA | 100 | 8.75 (d/t=0.5) | 24.71 |
| MNB | 200 | 8.75 (d/t=0.5) | 22.56 |
| MNC | 300 | 8.75 (d/t=0.5) | 17.65 |
| MND | 400 | 8.75 (d/t=0.5) | 18.14 |
| MNE | 600 | 8.75 (d/t=0.5) | 16.57 |


(a) (b)

Figure 1 Schematic illustrations of (a) smooth bar and (b) notched bar tensile specimens (units: mm).

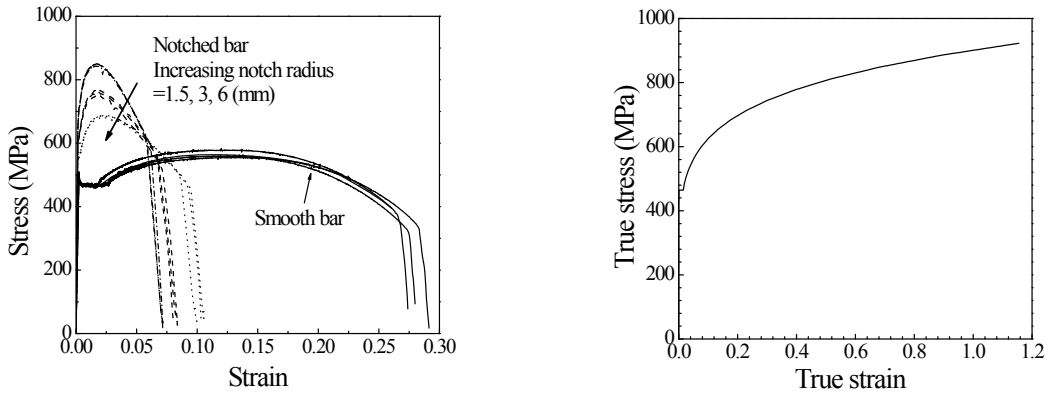


(a) (b)

Figure 2 (a) Engineering stress–strain curves from smooth and notched round bar tests, and (b) true stress–strain data.

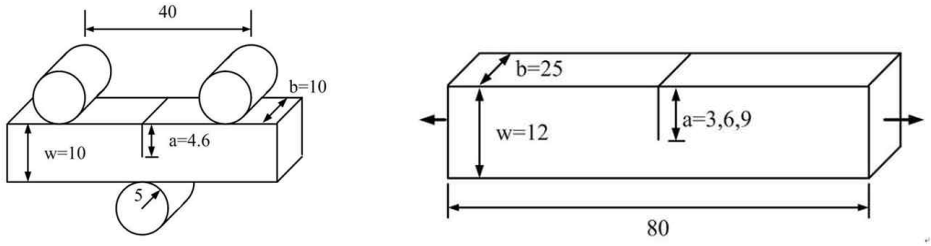


(a) (b)

Figure 3 Schematic illustrations of (a) SE(B) and (b) SE(T) specimens (units: mm).

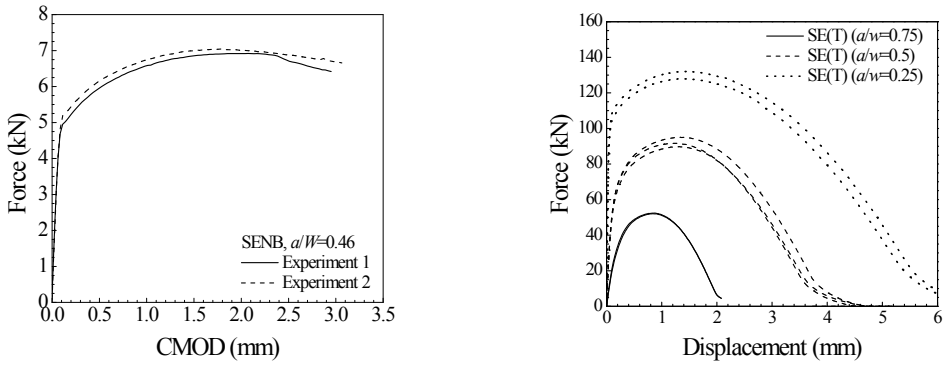


(a) (b)

Figure 4 (a) Experimental load-CMOD curves for SE(B) specimens, and (b) experimental load–displacement curves for SE(T) specimens.


(a) (b)

Figure 5 Gouge defect (a) before the test, and (b) after the test.

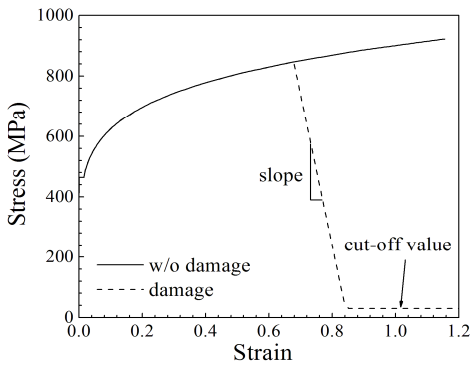


Figure 6 Schematic illustration of simulating ductile failure using stress relaxation.

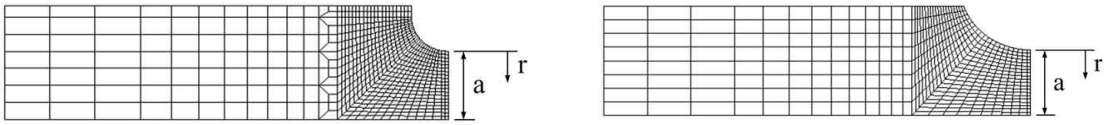


(a) (b)

Figure 7 FE meshes for notched tensile bars: (a) notch = 1.5 mm and (b) notch = 3 mm.

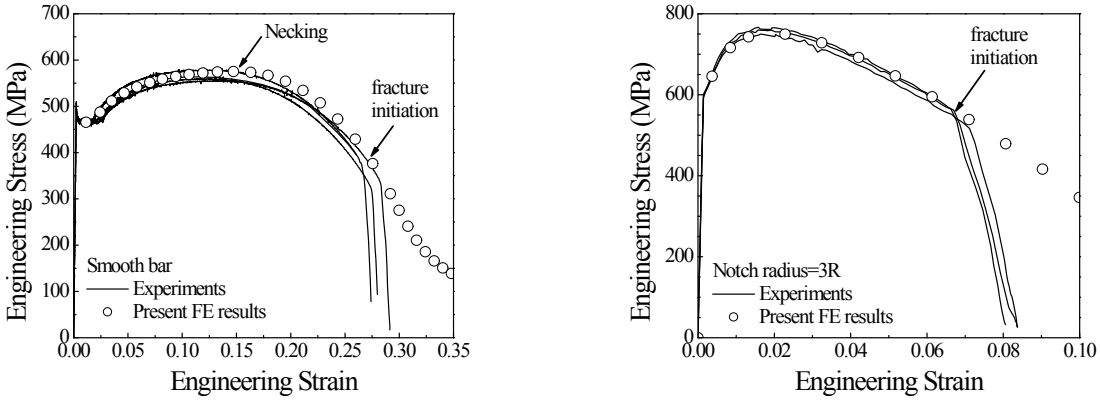


(a) (b)

Figure 8 Comparison of experimental engineering stress–strain data for (a) smooth and (b) notched (radius = 3 mm) tensile bars with FE results

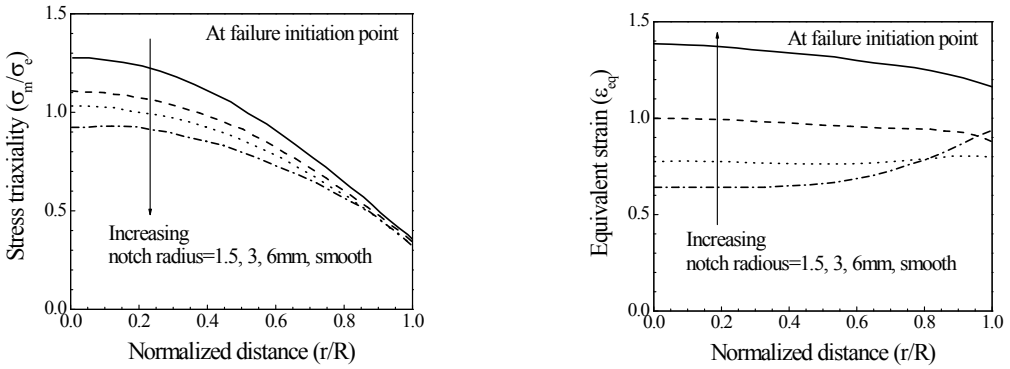


(a) (b)

Figure 9 (a) Stress triaxiality distributions and (b) equivalent strain distributions for smooth and notched tensile bars at the failure initiation point, determined from the FE analyses.

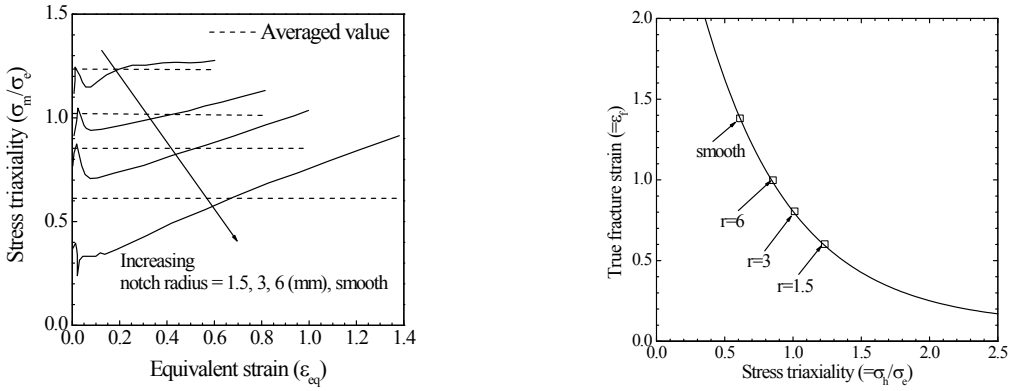


(a) (b)

Figure 10 (a) Variations of the stress triaxiality with the equivalent strain for smooth and notched bar tensile tests, and (b) fracture strain as a function of the stress triaxiality.

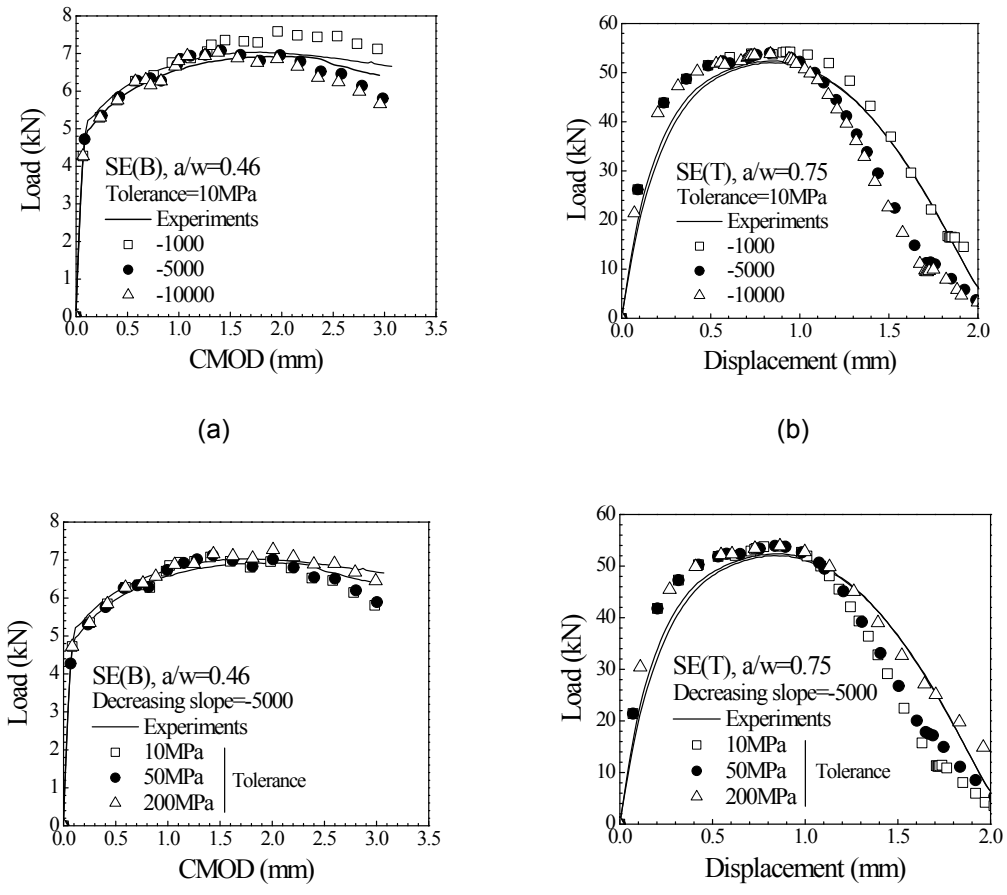


(a) (b)

(c) (d)

Figure 11 Sensitivity analysis results from 2-D SE(B) and SE(T) test simulations: (a) and (b) the effect of the decreasing slope; (c) and (d) the effect of the tolerance.

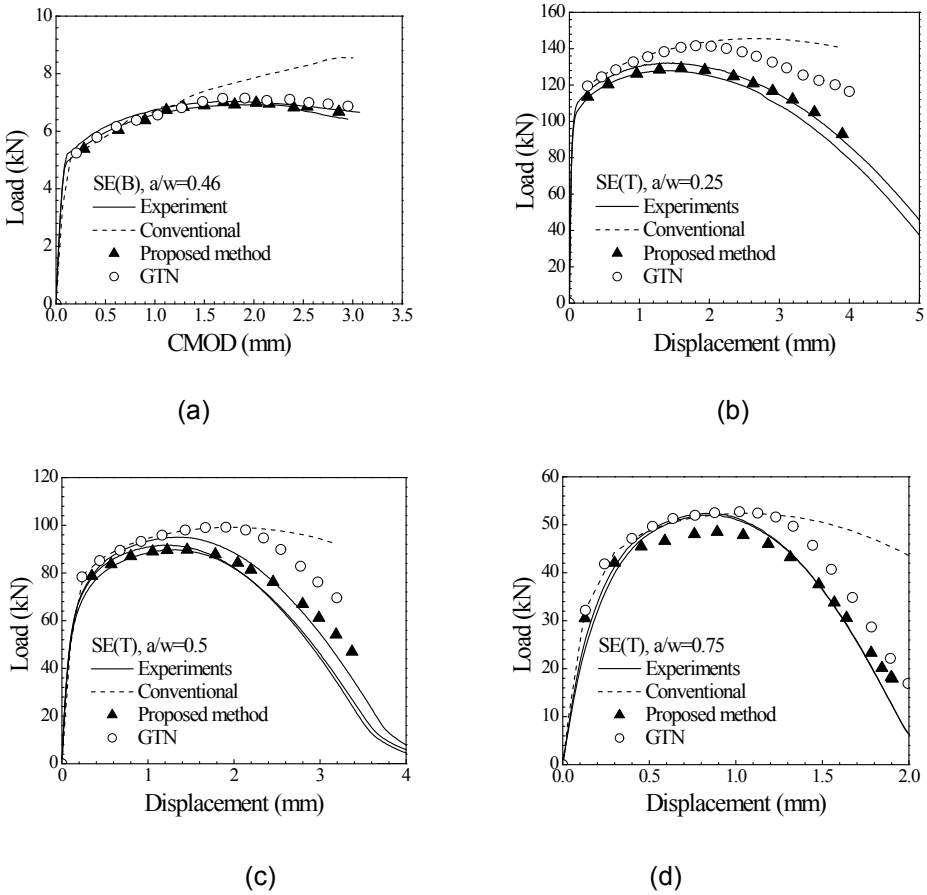


Figure 12 Comparison of cracked bar test results with simulated ones: (a) SE(B) with a/w=0.46; (b),(c) and (d) SE(T) with a/w=0.25, a/w=0.5 and a/w=0.75.

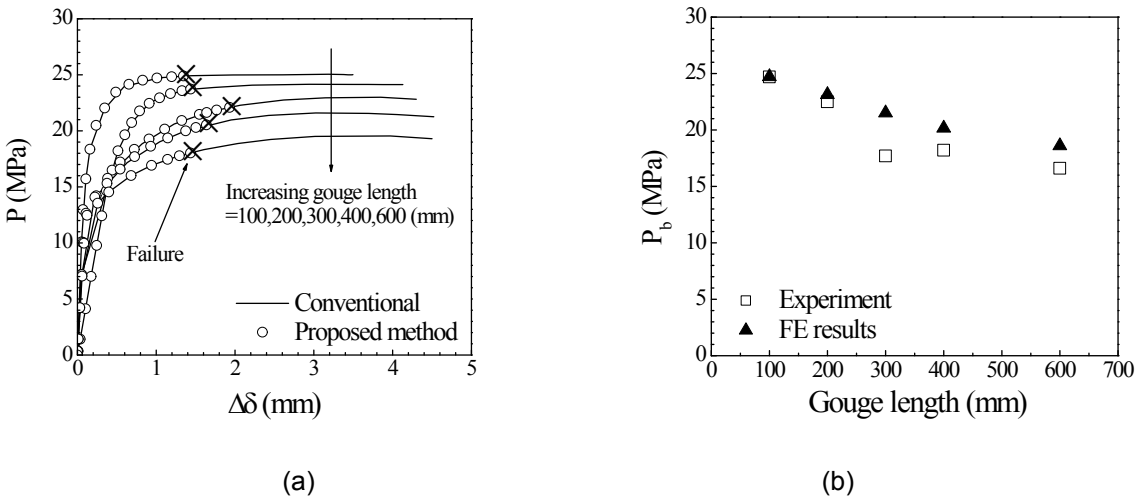


Figure 13 (a) FE pressure–displacement curves including predicted failure points, and (b) comparison of predicted burst pressures with experimental ones.